EXPERIMENTAL INVESTIGATIONS ON AN OGIVE-CYLINDER AT HIGH ANGLES OF ATTACK AND VARIOUS FREESTREAM CONDITIONS

K. Hartmann

Deutsche Forschungsanstalt für Luft- und Raumfahrt e.V.
Institut für Strömungsmechanik
D-37073 Göttingen, Bunsenstraße 10, Germany

Abstract

Subject of the experimental investigations was a slender cylindrical body with a three diameter long tangent-ogive nose. On this body of revolution force and moment -, pressure distribution -, and flow field measurements were carried out in two low speed wind tunnels in the incompressible speed range at angles of attack up to 90°. The Reynolds number and the body roll angle were varied systematically. In addition, flow visualizations were performed in a water towing tank and in the wind tunnel. The turbulence level in the wind tunnel was also changed. It was the objective of the investigations to get a better understanding of the complicated vortex flows over such a generic body geometry and to establish a data base for the development, improvement, and/or validation of any kind of prediction methods, nowadays increasingly more often CFD-codes upon the solution of the Euler or Navier-Stokes equations.

List of Symbols

B	unit length
$c_p = (p - p_\infty) / p_\infty$	surface pressure coefficient
$C_y = Y / (q_\infty \cdot S)$	total side force coefficient
$C_Z = Z / (q_\infty \cdot S)$	total normal force coefficient
$(c_y)_\ell = Y_\ell / (q_\infty \cdot D \cdot B)$	local side force coefficient
$(c_Z)_\ell = Z_\ell / (q_\infty \cdot D \cdot B)$	local normal force coefficient
D	body diameter
L	reference length related to wind tunnel nozzle exit, 3 m
Ma_∞, Ma	Mach number
p	static pressure on body surface
p_∞	freestream static pressure
$q_\infty = \frac{1}{2} \cdot \rho_\infty \cdot V_\infty^2$	freestream dynamic pressure
R = D/2	maximum body radius
Re_D, Re	Reynolds number, based on body diameter
r(x)	local body radius
$S = (\pi D^2) / 4$	reference area
Tux, Tuy, Tuz	turbulence levels in x, y, z direction, respectively
U_∞, V_∞	freestream velocity
u', v', w'	fluctuating part of velocity components in x, y, z direction, respectively
V_{yz}	velocity component in the cross-flow plane yz
x, y, z	cartesian coordinates
x_{CP}	center of pressure of normal - and side force, distance from nose tip
Y, Y_ℓ	total or local side force coefficient, respectively
Z, Z_ℓ	total or local normal force coefficient, respectively
α	angle of attack
Φ	body roll angle about longitudinal axis, $\Phi = 0°$ arbitrary
Θ	angular position on body surface relative to wind ward generator, positive anticlockwise looking at body base
ρ_∞	freestream density

1. Introduction

The body in Fig. 1 represents a generic geometry for missiles, rockets, front part of fuselages of fighter aircrafts etc.. Experimental data of its flow field are more and more required for the validation of CFD-codes, based for example on the solution of the Euler or Navier-Stokes equations. Other methods are of course not excluded. A comprehensive data base, obtained in two low speed wind tunnels of the same kind and in a water towing tank, contributes to this purpose and provides also a better understanding of the flow over such bodies. At high angles of attack, in case of the present paper up to 90°, the flow around such a geometry is governed by different types of flow separation (laminar, transitional, turbulent boundarys layers) leading to extremely 3D vortex flows of various structures. The dominant flow phenomenon is the occurrence of lateral forces with random sign even at zero sideslip which in practice leads to severe control problems. The local force distributions and overall forces as integral values of the surface pressures depend, apart from the geometry, on the angle of attack, the Reynolds and Mach number, the level and structure of the freestream turbulence and the body roll orientation. For that reason an exclusively theoretical treatment of such

flow fields is for all freestream conditions till today not possible and remains a great challenge for every CFD activity.

A systematic experimental data base serves also the improvement or development of fast semiemperical and inexpensive engineering prediction methods which are required for the conceptual design of missile systems. Such methods have to provide highly accurate preliminary estimates of aerodynamic performance, stability and control. The most commonly used type of such methods is the so-called component build up method which adds up the forces acting on each individual component of a missile (body, wing, tail) and takes into account interference loads. In this connection the circular cylinder body of a missile is the most complicated component because the positions of the separation lines are not known a priori, because of the absence of sharp edges, but evolve from the interaction between the boundary layer and the outer flow.

2. Experimental arrangements

2.1 Models

For the different kinds of experiments three models of nominally the same geometry were manufactured. A high length-to-diameter ratio (L/D = 11 for the force model, L/D = 14 for the pressure model) was desired to study the flow development over a large distance along the body. The diameter of the wind tunnel models was chosen to D = 200 mm in order to achieve Reynolds numbers as high as possible at the maximum speed of the two available wind tunnels. Limitations of the dimensions were given by the size of the test sections. For the force measurements with an internal balance a separate model was made with a very smooth surface in order to avoid any possible disturbing influence of pressure holes. The model for the pressure measurements is by 3D longer than the force model because the influence of the body base should be kept away from the last pressure section. Steady pressure distributions on the model surface were measured in the conventional way via pressure taps, rigid and flexible tubes, pressure transducers and scanivalves. The arrangement of the pressure taps and the model geometry is given in Fig. 1. For unsteady pressure measurements a total of 32 Kulite pressure transducers were arranged in two cross sections as will be described later together with the results of the unsteady pressure measurements.

By a factor 5 smaller model was fabricated of plexiglas for the flow visualizations with hydrogen bubbles in a water towing tank.
Five somewhat different, but similar, sting supports were used to install the two models in the test sections and because of the splitting of the whole angle of attack range into a lower and upper one. Fig. 2 shows the supports I, II and III. In case of the force model the angle of attack was set in a horizontal plane.

2.2 Wind tunnels

The tests were carried out in two similar open jet low speed wind tunnels of the DLR at Göttingen (designated as NWG, test section size 3 m x 3 m)[1,2] and at Braunschweig (designated as NWB, test section size 2,8 m x 3,25 m)[3,4]. Sketches of the test sections and the arrangement of the model for the pressure measurements are given in Figs. 3 and 4. The boundaries of the mixing zones of the open jets of the test sections are indicated in these figures. Care was always taken to keep the model inside of the undisturbed region of the open jet, except a part of the rear of the body which was not pressure instrumented. In order to achieve this, the support with the model was, at angles of attack greater than 60°, shifted vertically to a lower position.

Investigations of the flow quality of both wind tunnels were conducted by E. Fröbel and U. Michel[5,6]. Among other features of the test sections also the turbulence levels were determined. The results, given in Fig. 5, show a higher turbulence level in the Göttingen tunnel, NWG.

2.3 Test program

The force and steady pressure measurements comprise angles of attack from 0° to 90° and Reynolds numbers of 2.5×10^5, 3.7×10^5 and 7.7×10^5 (based on body diameter and freestream conditions). In a few selected cases this range was extended to 1.3×10^5 to 11×10^5. At angles of attack greater than 20° the dependence on the body roll position was investigated systematically with a complete coverage of 360°. The force measurements in the Göttingen tunnel, NWG, were carried out at different turbulence levels which were changed by applying turbulence grids at the nozzle exit.

The body vortices were visualized in a water towing tank[7] using hydrogen bubbles and in the Braunschweig tunnel, NWB, with the aid of smoke and a laser light sheet. The latter tests were carried out simultaneously with the pressure measurements, i.e. at the same flow conditions.

In a limited extent flow field measurements, using a 9-hole probe, were performed at angles of attack less than 30° in several cross flow planes.

The steady pressure measurements were completed by unsteady pressure measurements in a restricted scope for certain flow conditions in the cross sections at x/D = 5 and 11.

The whole test program is compiled in Table 1.

Table 1: Test program

α [deg.]	V_∞ [m/s]	$Re_D \times 10^{-5}$	Φ [deg.]	Wind Tunnel	Remarks
Flow visualizations					
$0 \rightarrow 90$	0.125	0.05	0	water towing tank	hydrogen bubbles plexiglas model D = 40mm L/D = 15
35 55 55	5, 10, 20, 40 20 20	0.63, 1.25, 2.5, 5 2.5 2.5	0 0, 120 0 to 360, $\Delta\Phi = 60$	NWG	smoke and laser light sheet x/D = 6.25 x/D = 1 to 10 x/D = 3
Total force measurements (1.5" TASK balance)					
$0 \rightarrow 90$ $90 \rightarrow 0$	11, 21, 40, 58	1.4, 2.6, 5.2, 7.6	0	NWG	without and with turbulence grid
Steady surface pressure measurements					
$0 \rightarrow 90$ $\Delta\alpha = 5$	20, 30, 60	2.5, 3.8, 7.4	0	NWG	
20, 30, 40 50, 60, 70	20, 60	2.5, 7.4	$0 \rightarrow 360$ $\Delta\Phi = 30$		
25, 35, 45, 55 65, 75, 85, 90	20, 30, 60	2.5, 3.7, 7.4	$0 \rightarrow 360$ $\Delta\Phi = 30$	NWB	
Flow field measurements (9-hole pressure probe)					
30, 40, 60	21, 32, 42, 63	2.6, 3.9, 5.2, 7.8	0	NWG	cross sections at x/D = 5, 7 and 9
Unsteady surface pressure measurements (Kulite pressure transducers)					
$0 \rightarrow 90$ $\Delta\alpha = 10$	32, 63	3.9, 7.8	0	NWG	without and with turbulence grid

Annotation: NWG = 3 m low speed wind tunnel of the DLR at Göttingen
NWB = 3 m low speed wind tunnel of the DLR at Braunschweig

3. Results

3.1 Flow Visualizations

Although the experiments in the water towing tank could only be carried out at a Reynolds number much smaller than in the wind tunnel, the results provide an excellent idea of the flow phenomena. The examples of the results in Fig. 6 demonstrate the classification of there basic flow regions within the whole incidence range from 0° to 90° as follows: Fig. 6a, symmetric / steady vortex structure; Fig. 6b, asymmetric / steady vortex structure; Fig. 6c, asymmetric / unsteady vortex structure and approaching the 2D circular cylinder case, except the nose and base region of the body.

The flow visualization in the wind tunnel by the aid of smoke and a laser light sheet was performed in such a manner that the light sheet was either kept at a certain cross section during the change of the incidence or traversed along the body at a constant angle of attack. The visualized vortex patterns were recorded by a video-camera and the video tape was afterwards used for the image processing. These visualizations and the analysis of the results were carried out in cooperation with J. Kompenhans. The results are documented in[8]. One example is given in Fig. 7 which shows the alternating vortex positions in three planes (side view, plan view, sectional view) and a comparison with calculations from D. Nikolitsch, DASA, Ottobrunn. The calculations were made on the basis of a multi-vortex model at which the side of the first vortex separation was adapted to the experiment. For the rest the agreement is very good.

3.2 Total force coefficients from balance measurements

The complete results are documented in [9]. Selected examples are depicted in Figs. 8a to 8c. All force coefficients reveal a strong non-linear characteristic with the angle of attack. The nominal Reynolds number was varied by changing the freestream velocity. Laminar, transitional and turbulent boundary layer conditions and separations are included in the present Reynolds number range. Except the highest Reynolds number, the forces were measured at both increasing and decreasing angles of attack with a good agreement. The onset of the flow asymmetry, coupled with the occurrence of side forces, is independent of the Reynolds number and begins at α about 20°. At all Reynolds numbers the side forces are greatest at incidences around 50°. Maximum side forces were obtained at the transitional Reynolds number of Fig. 8b. The increased turbulence levels, caused by a grid, resulted in a strong reduction of both the normal and side forces at transitional and smaller Reynolds numbers. At higher Reynolds numbers this effect is reversed, see Fig. 8c. This behaviour is related to the Reynolds number

dependence of the circular cylinder drag which corresponds to the body cross forces. Concerning the Reynolds number it should be pointed out here that a so-called effective Reynolds number is a much better flow parameter for the interpretation of the results. Such an effective Reynolds number is defined with a characteristic length which takes into consideration the physically relevant streamline of the fluid particles from the stagnation line to the separation position. This characteristic length depends of course on the angle of attack.

3.3 Steady pressure distributions

The results of the static pressure measurements form the main data body of the whole investigations. The entirety of the data are documented as pressure coefficients in form of numerical lists and different kinds of plots in internal DLR reports[9,10,11,12]. In addition, the data are available on a computer tape. For the illustration of the most important features of the pressure distributions the series of Figs. 9 to 13 for $\alpha = 55°$ and $\Phi = 0°$, reflecting the nearly most complex flow field, were selected to be discussed here. This series covers a Reynolds number range which includes all types of boundary layers (laminar, transitional, mixed and turbulent) and the accompanying flow separation. The lee side vortex structure at $\alpha = 55°$ is that of Figs. 6b and 7, characterized by the alternating vortex separations along the body. This process and the resulting flow field is, disregarded small turbulent fluctuations, yet steady in comparison with the conditions at higher angles of attack. The actual roll angles are of course arbitrary. Therefore the position $\Phi = 0°$ was at the beginning of the tests once marked on the body to be coincident with the stagnation line. It should be emphasized here that the asymmetric vortex patterns, arising from an originally symmetric attitude, are caused by unstable interactions of the closely positioned vortices with each other and the body. These process may be dominantly affected and controlled by turbulence spots of the freestream, different boundary layer transitions and separations on opposing sides of the body and geometric nose tip imperfection, i.e. any deviations from an ideal rotary geometry. For this reason a systematic variation of the body roll position was desirable and therefore carried out.

The Figs. 9 to 12 show pressure distributions for the four Reynolds numbers of $Re_\infty \times 10^{-5} = 1.3, 2.5, 3.7$ and 7.3 at fifteen cross sections along the body. Because the body sectional forces can be related to the drag of the circular cylinder, the knowledge of it can be used to interpret the present pressure distributions. At the two smaller Reynolds numbers the generally low amount of pressure recovery on the lee side before separation indicates the laminar case, leading to more or less "flat" pressure distributions with different magnitudes on both sides. The results of the next higher Reynolds number $Re_\infty = 3.7 \times 10^5$, obviously a transitional one, show mainly laminar separation on one side and turbulent separation on the opposite side. We find exclusively turbulent separation at the highest Reynolds number $Re_\infty = 7.3 \times 10^5$. At this Reynolds number the pressure distributions become, very soon behind the ogival nose, more and more symmetric. In all other cases we find a strong asymmetry in the pressure distributions caused by the asymmetric vortex structures. This asymmetry is stronger in the forward part of the body because here the vortices are closer to it and their velocity and pressure induction on the body surface is more pronounced. Along the body one can recognize a change of the asymmetry which correlates with the alternating vortex separation as to be seen in Figs. 6 and 7.

The pressure measurements of Figs. 9 to 12 were repeated several times at each Reynolds number. Between these individual tests either measurements at other angles of attack and Reynolds numbers were carried out or the wind tunnel was stopped and newly started. In spite of this changes the pressure distributions at each Reynolds number make evident a distinct repeatability. Thus, one can conclude that the data are very reliable, especially with regard to the vortex asymmetry. This statement is of course only valid for the conditions with the individual model in this wind tunnel, but not yet of general validity.

Results obtained at the maximum Reynolds number of $Re_D = 11 \times 10^5$, not presented in this paper because of the limitation of its size, differ from those of $Re_\infty = 7.3 \times 10^5$ only qualitatively with a similar characteristic.

Fig. 13 shows results from the Göttingen tunnel for nominally the same freestream conditions as in the Braunschweig tunnel, see Figs. 10 to 12. In the test section of the Göttingen tunnel the turbulence level is much higher than in the Braunschweig tunnel. The flow quality on the whole is in the former not very good with the consequence that the transitional Reynolds number is much smaller. At the two higher Reynolds numbers we find in all cross sections turbulent separation with almost no asymmetry. The pressure distributions of the smallest Reynolds number feature turbulent separation on the nose with a weak asymmetry. Short behind the nose the pressure distribution becomes asymmetric over a short distance of the body with laminar separation on one side and turbulent on the opposite side. The asymmetry disappears and changes into symmetrically laminar separation. At the smallest Reynolds number it was found, of course only in this special case, along the body at first turbulent, then mixed and further downstream laminar separation. This specific feature of the pressure distribution was not expected and is therefore really worth noting.

The alternating vortex separation leads to a cyclic nature of the local side forces along the body as illustrated in Fig. 14. Results from a cooperation with an AGARD working group are compared in this figure. The measurements have been performed in different wind tunnels of different turbulence levels. For this comparison roll angles have been selected which resulted in equivalent side force distributions. The first maximum side force was found around the axial position $x/D = 4$. Fig. 15 shows the corresponding pressure distributions which illustrate how on opposing sides of the body the pressure coefficients can exhibit either only laminar separation or can be varied with obviously different characteristics of turbulent reattachment and subsequent separation. These differences are then reflected in the changes of the local side force coefficient values. There is a greater re-

semblance between the ONERA and DLR than with these data to the BAe ones. This indicates that a small increase of Reynolds number from 1 to 2.4 or 2.8 x 10^5, in the case of DLR and ONERA respectively, has been sufficient to change the flow character from laminar to a mixed laminar/turbulent flow type. The latter happened on the side where one of the asymmetric vortices is closer to body and thereby inducing higher velocities and lower pressures with distinct pressure peaks.

The influence of the roll angle is demonstrated in Fig. 16 in which pressure distributions of equivalent asymmetry are compiled with the roll angle as parameter. The two groups illustrate opposite asymmetry. There are no or only very small differences among the pressure distributions of the group on the right side of Fig. 16. The group on the lift side of Fig. 16 shows, at least for the more forward sections,somewhat greater differences between the single pressure distributions. It is very difficult to give a convincing explanation for these results. Nevertheless, when the asymmetry is achieved, the data are predominantly reproducible.

Two groups of pressure distributions from both wind tunnels are compiled in Fig. 17 by which the repeatability is demonstrated. The group on the left side of Fig. 17 was obtained in the Braunschweig tunnel. Between the several run numbers either tests at other freestream conditions were performed or the tunnel was stopped and started again. The agreement among one another is with respect to all features quite good. Even better is the agreement of the group on the right side of Fig. 17 which represents results from the Göttingen tunnel with the higher turbulence level. This group of pressure distributions was obtained at different sampling times and measured successively without any change of the nominal freestream condition. There is no evidence of instability. The very good repeatability of the measurements make evident that the data are reliable.

3.4 Local force distributions

From the pressure distributions local normal force and local side force distributions were determined by integration of the pressure distributions applying the relatively simple trapezoid rule. The following formulas are valid and were used:

$$(c_Z)_\ell = \frac{1}{2R}\int_o^{2\pi} c_p \cos\Theta \; r(x)\, d\Theta$$

$$(c_y)_\ell = -\frac{1}{2R}\int_o^{2\pi} c_p \sin\Theta \; r(x)\, d\Theta$$

Figs. 18 and 19 show example distributions of local normal and side forces for two Reynolds numbers and a complete body roll sweep of 360°. In these figures the results from the two wind tunnels at Göttingen and Braunschweig are compared. These local force distributions reflect the effect of the body roll angle. Although the repeatability of the pressure measurements in either tunnel is very good, the cyclic characteristics of the local side forces do not agree completely in every case. Also the local normal forces show some disagreements. At the higher Reynolds number the local normal forces are smaller than at the lower one because of turbulent separation. The local side forces are also smaller at the corresponding Reynolds number and diminish strongly or disappear, respectively, behind the nose region.

3.5 Total forces derived from pressure distributions

The total normal and side forces were determined by a twofold integration of the surface pressure distributions using the following formulas:

$$C_Z = \frac{Z}{q_\infty S} = \frac{1}{q_\infty S}\int_o^{L^*}\int_o^{2\pi} (p - p_\infty)\cos\Theta \; r(x)\, d\Theta\, dx$$

$$C_Y = \frac{Y}{q_\infty S} = -\frac{1}{q_\infty S}\int_o^{L^*}\int_o^{2\pi} (p - p_\infty)\sin\Theta \; r(x)\, d\Theta\, dx$$

L^* is the length from the body nose tip to the last cross section equipped with pressure taps.

For the three main Reynolds numbers of the tests the results from both wind tunnels are plotted as function of the angle of attack for the body roll angle Φ = 0° in Figs. 20 to 22. The variation of the forces with the roll angle are indicated in these figures by vertical lines, i.e. double arrows and bars. At the roll angel Φ = 0° the normal forces, measured in the Göttingen tunnel, are at subcritical and critical Reynolds numbers smaller than in the Braunschweig tunnel and vice versa at supercritical Reynolds numbers, except the range of moderate angles of attack. This effect is apparently caused by the higher turbulence level of the former tunnel which simulates higher Reynolds numbers leading to earlier boundary layer transition and thereby to smaller forces in the critical Reynolds number range, and higher forces in the supercritical and transcritical Reynolds number range.

The side forces are greatest at angles of attack between about 50° to 70°. They show in this range also the greatest variation with the roll angle at the critical Reynolds number and achieve here values which are greater than the normal forces.

Figs. 23 and 24 demonstrate the Reynolds number dependence of the normal and side force coefficients and their centers of pressure for the freestream conditions (α = 55°, Φ = 0°) of the pressure distributions of Figs. 9 to 13.

The variation of the side forces with the roll angle is illustrated in Figs. 24 and 26. These show a wavelike characteristic of the results from both wind tunnels with a much more regular tendency of the results from the Braunschweig tunnel, presumedly because of the lower turbulence level in this test section. In both tunnels the highest side forces were found at the critical Reynolds number which is, as already explained, apparently somewhat lower in the Göttingen tunnel. The positive and negative side forces are shown to be equal in the case of the regular characteristic.

3.6 Flow field measurements

In several crossflow planes, i.e. planes perpendicular to the body length axis, the velocity vectors were determined by pressure measurements with a conventional 9-hole pressure probe. This probe was mounted on a special rig and traversed along parallel lines in the crossflow planes. An example of the results is given in Fig. 27. The arrows

represent the projections of the velocity vectors to the crossflow plane. The end of each arrow coinsides with the measuring location and the arrow length represents the amount of the velocity component. At the moderate angle of attack of $\alpha = 30°$ it is clearly to recognize that the two vortices are already located symmetrically. The complete data are documented in [13,14].

3.7 Unsteady pressure measurements

These measurements were performed in close cooperation with colleagues from the Institute of Aeroelasticity of the DLR at Göttingen. These people made available their data acquisition and processing equipment and helped to asses the data. The tests were carried out in a restricted scope and must be considered as a completion of all other experiments, especially the steady surface pressure measurements. Examples of the results are given in Figs. 28 to 33. Fig. 28 shows six different traces of the dynamic part of the surface pressure recorded by Kulite pressure transducers. Opposite pressure tap locations on the body circumference were selected close to the boundary layer separation location as can be deduced from the pressure distributions depicted on the top right corner of Fig. 28. At both example angles of attack, $\alpha = 35°$ and 37.5°, in the forward cross section A-A the frequency on one side is clearly higher than on the opposite side, reflecting the asymmetry. In the more downstream cross section B-B the frequency as well as the amplitudes are much higher than in the upstream location.

A complete set of pressure traces around the body circumference is given in Fig. 29 for the extreme angle of attack $\alpha = 90°$. Also in this case the strongest signals were obtained at corresponding pressure tap locations. The $\alpha = 90°$ case can be compared with the 2D case of a circular cylinder.

All measured pressures were processed on the basis of a Fourier analysis. The results are represented as power spectra. Examples are given in Figs. 30 to 33.

3.8 Accuracy estimates

In accordance with the management and the responsible experts of the DLR's wind tunnel department the following statements can be made with respect to the tolerance of the freestream velocity and the accuracy of the measured quantities. The uncertainty of the freestream velocity V_∞ is $\pm$ 0.25% and the angle of attack could be set geometrically with an accuracy of $\Delta\alpha < \pm 0.1°$.

The force and moment measurements with the balance are more inaccurate because a very rigid strain gauge balance had to be used and its high load range was not utilized by the relatively small aerodynamic forces in comparison to the model weight. Tolerances are as follows:

Normal force	$\pm$ 1%
Side force	$\pm$ 4%
Axial force	$\pm$ 3%
Pitching moment	$\pm$ 2%
Yawing moment	$\pm$ 7%

All values mentioned above are related to induvidual maximum measured steady forces or moments, respectively.

In the case of flow field measurements an error of $\pm$ 0.25% of V_∞ is valid for the amount of the velocity components. The flow direction can be determined within an error band of less than 0.1° at velocities greater than 20 m/s, but increasingly higher at smaller velocities.

4. Summary and conclusion

Some selected results of flow visualizations, force, pressure and flow field measurements on an ogive-nosed circular cylinder body were presented. The complete data are documented in several internal DLR reports. It is worth noting that in addition to the geometric and freestream parameters the turbulence level and structure of the test sections has also to be taken into account to obtain reliable data. In particular, the pressure measurements with the same model in two similar wind tunnels are shown to be repeatable in each tunnel, but the corresponding results from both tunnels don't agree one with another in every case. They reveal partly more or less greater differences, presumedly caused by the different turbulence levels in the two tunnels. Nevertheless, on the whole the data are reliable and form a comprehensive and good basis for the assessment of every kind of prediction methods and in addition for the validation of CFD codes.

References

(1) W. Baumert et al.: Der 3 m x 3 m Niedergeschwindigkeits-Windkanal (NWG) in Göttingen (Stand 1988) DFVLR-Mitt. 89-05, 1989

(2) G. Kausche, H. Otto, D. Christ und R. Siebert: Der Niedergeschwindigkeits-Windkanal der DFVLR in Braunschweig, DFVLR-Mitt 88-25, 1988

(3) A. Kühn: Strömungsfeldmessungen im 3 m x 3 m Niedergeschwindigkeits-Windkanal (NWG) der DFVLR in Göttingen, DFVLR-Mitt. 85-14, 1985

(4) R. Siebert: Druckmeßtechnik in der Hauptabteilung Windkanäle der DFVLR (Stand 1988), DFVLR-Mitt 88-11, 1989

(5) E. Fröbel: Vergleichende Turbulenzmessungen in Großwindkanälen, DFVLR IB 357 - 75/1

(6) U. Michel, E. Fröbel: Aerodynamic Data Accuracy and Qualitiy: Requirements and Capabilities in Wind Tunnel Testing, AGARD Conference Proceedings No. 348, 1988

(7) H. Bippes, P. Colak-Antic: Der Wasserschleppkanal der DFVLR in Freiburg i. Br., ZWF 21, Heft 4, 1973, S. 113-120

(8) J. Kompenhans, K. Hartmann: Strömungssichtbarmachung an einem hochangestellten Ogivkreiszylinderrumpf mit Hilfe der Laser-Lichtschnittmethode DFVLR - FB 86-45, 1986

(9) K. Hartmann: Einfluß der Reynoldszahl und der Windkanalturbulenz auf die aerodynamischen Beiwerte von Flugkörperrümpfen bei Anstellwinkeln bis zu 90°, DFVLR IB 222 . 84 A 30, 1986

(10) K. Hartmann: Pressure and force distributions on an ogive-nosed circular cylinder at high angles of attack in an incompressible airstream
DFVLR IB 222 - 83 A 05, 1983,
DFVLR IB 222 - 83 A 05a; data lists, part I, 1983,
DFVLR IB 222 - 83 A 05b; data lists, part II, 1983

(11) W. Hastreiter: Druckmessungen an einem Kreiszylinder-Rumpf mit Ogivalspitze,
DFVLR - IB 19111 - 83 C 19, 1983
Teil I: Diagramme für $\alpha = 0°$ bis 35°
Teil II: Diagramme für $\alpha = 35°$ bis 60°
Teil III: Diagramme für $\alpha = 65°$ bis 85°
Teil IV: Diagramme für $\alpha = 90°$
Teil V: Ergebnistabellen für Versuchsnr. 1 bis 232
Teil VI: Ergebnistabellen für Versuchsnr. 325 bis 565

(12) K. Hartmann: Data from pressure measurements on an ogive circular cylinder body at incidences up to 90°,
DLR IB 223 - 94 A 03, 1994 Volume I,
DLR IB 223 - 94 A 04, 1994 Volume II

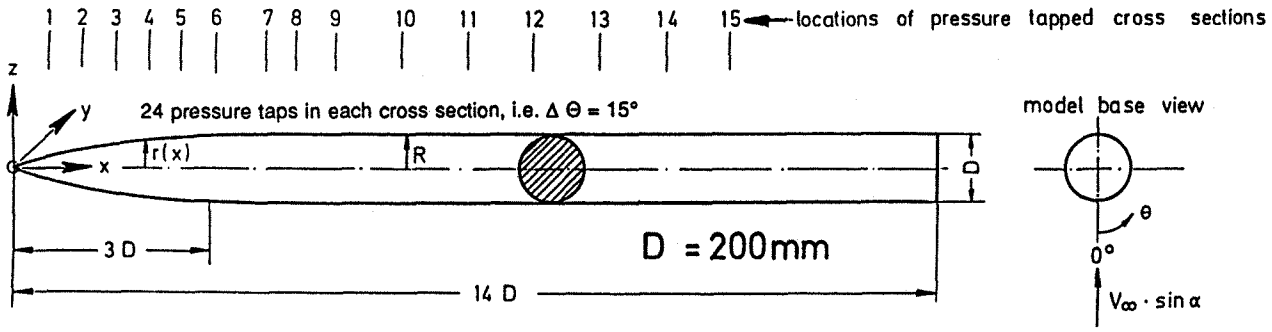

coordinates of pressure tapped cross sections:

cross section	1	2	3	4	5	6	7	8	9	10	11	12	13	14	15
$\frac{x}{D}$	0.525	1.025	1.525	2.025	2.525	3.025	3.775	4.225	4.825	5.825	6.825	7.825	8.825	9.825	10.825

contour of model nose: $\frac{r(x)}{D} = 0.309840 \cdot \left(\frac{x}{D}\right) - 0.039867 \cdot \left(\frac{x}{D}\right)^2 - 0.002615 \cdot \left(\frac{x}{D}\right)^3$

Fig. 1: Model geometry and positions of pressure tapped cross sections

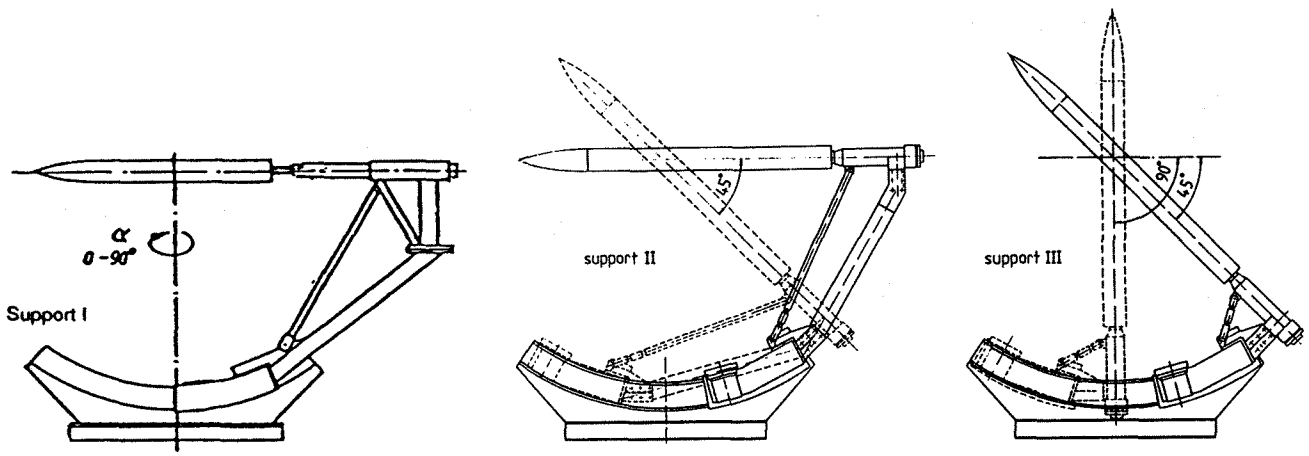

Fig. 2: Different sting supports for force (support I) and pressure measurements (supports II and III)

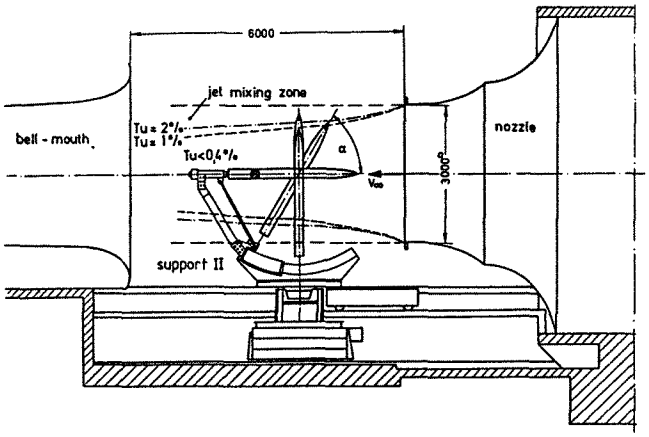

Fig. 3: Model in the working section of the 3 m low speed wind tunnel (NWG) of the DLR at Göttingen. Different extreme model positions are depicted

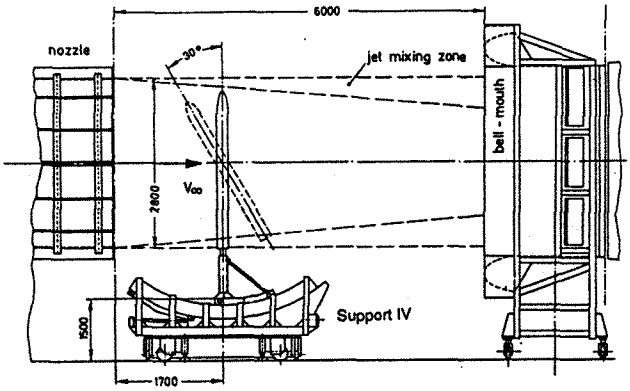

Fig. 4: Model in the working section of the 3 m low speed wind tunnel (NWB) of the DLR at Braunschweig

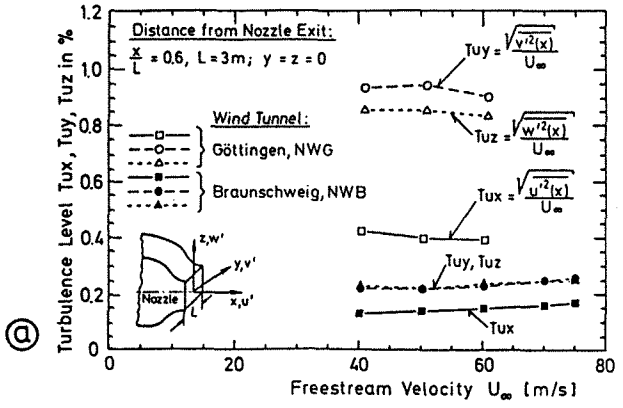

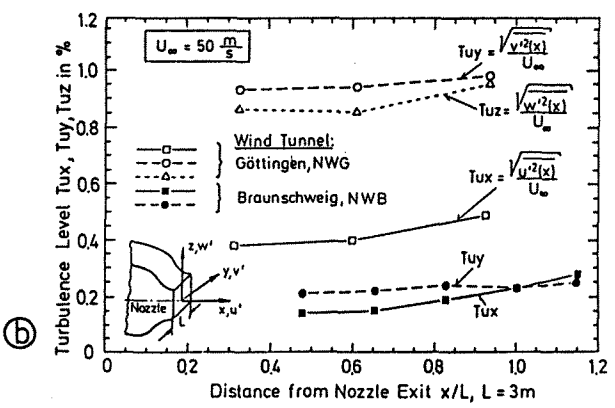

Figs. 5a and 5b: Turbulence levels of the two 3 m low speed wind tunnels of the DLR at Braunschweig and Göttingen. Results from U. Michel and E. Fröbel, DLR, SM-ES-B, Berlin

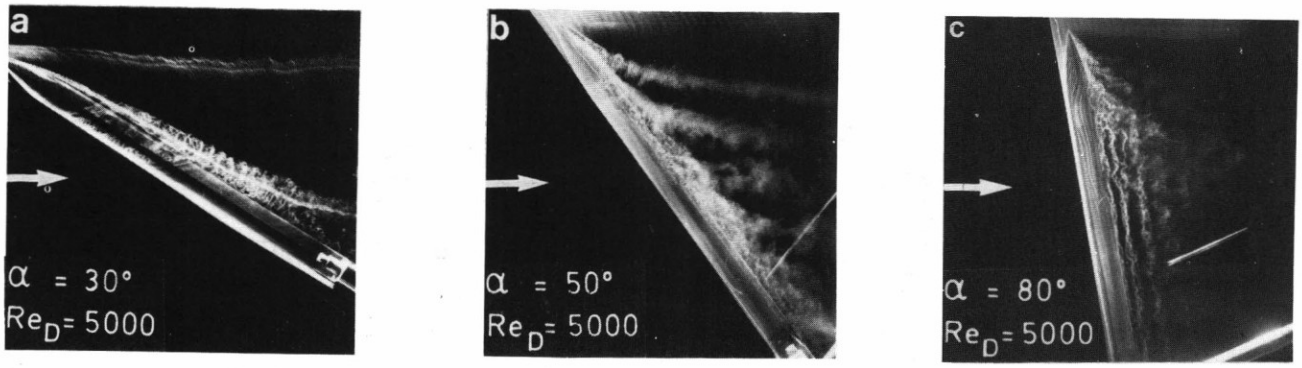

Fig. 6a to 6b: Vortices visualized in a water towing tank using hydrogen bubbles

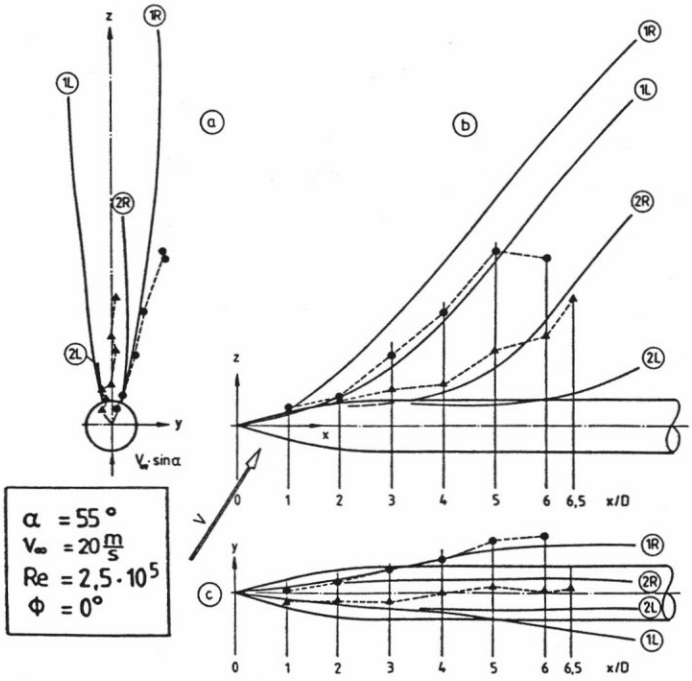

Fig. 7: Vortex positions in different planes (a, b, c)

_____Experiment; visualization by smoke and laser light sheet
--------Calculation; results from D. Nikolitsch, DASA, Ottobrunn

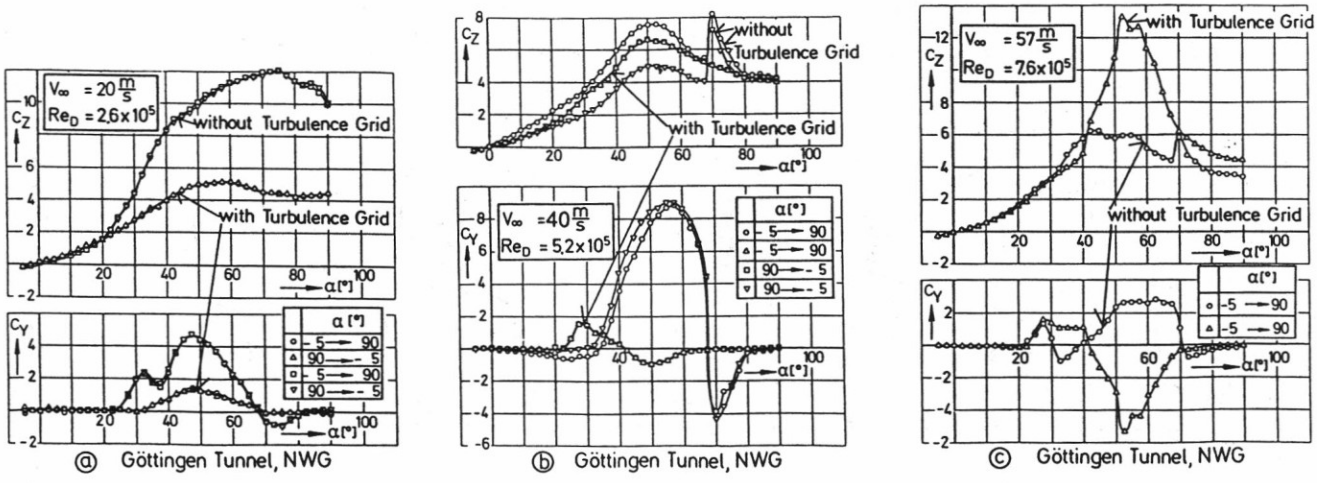

Figs. 8a to 8b: Total normal and side force coefficients (balance measurements)

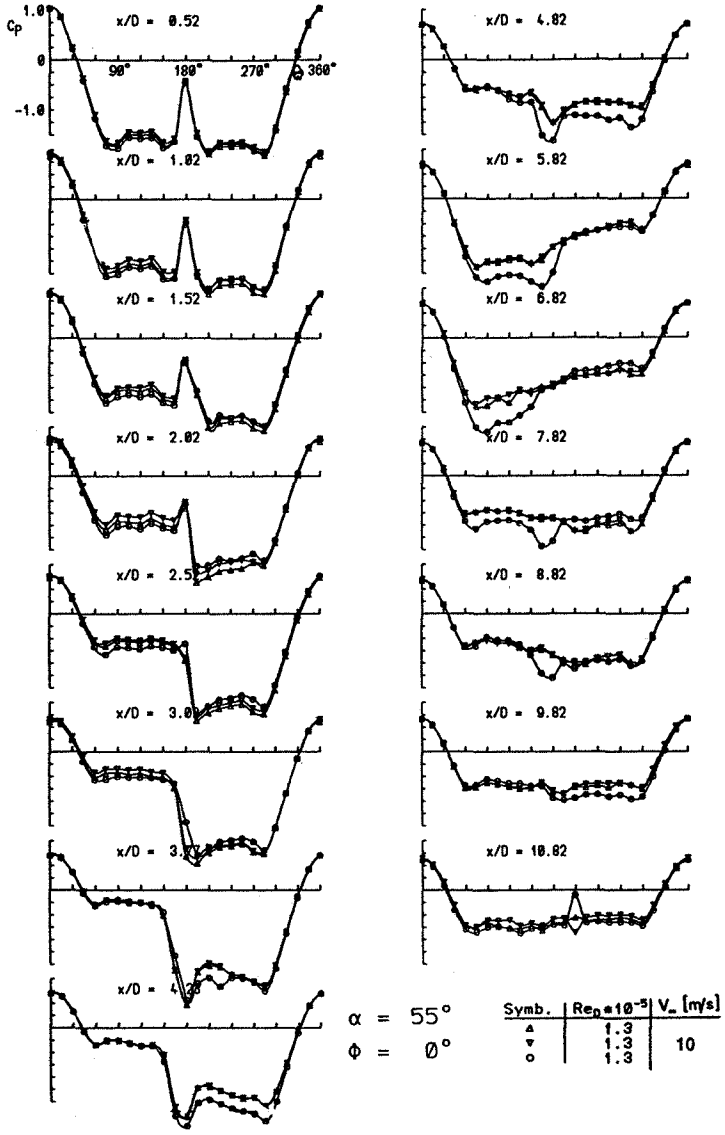

Fig. 9: Surface pressure distributions in 15 cross sections along the model. Results from the low speed wind tunnel NWB at Braunschweig

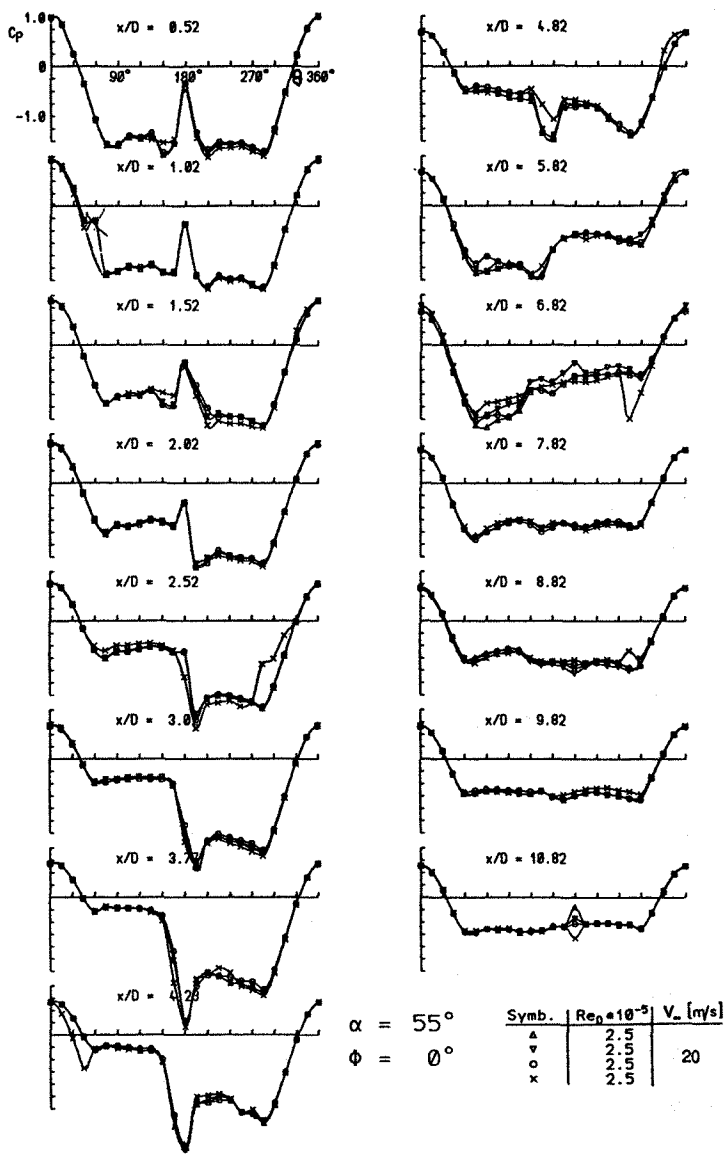

Fig. 10: Surface pressure distributions in 15 cross sections along the model. Results from the low speed wind tunnel NWB at Braunschweig

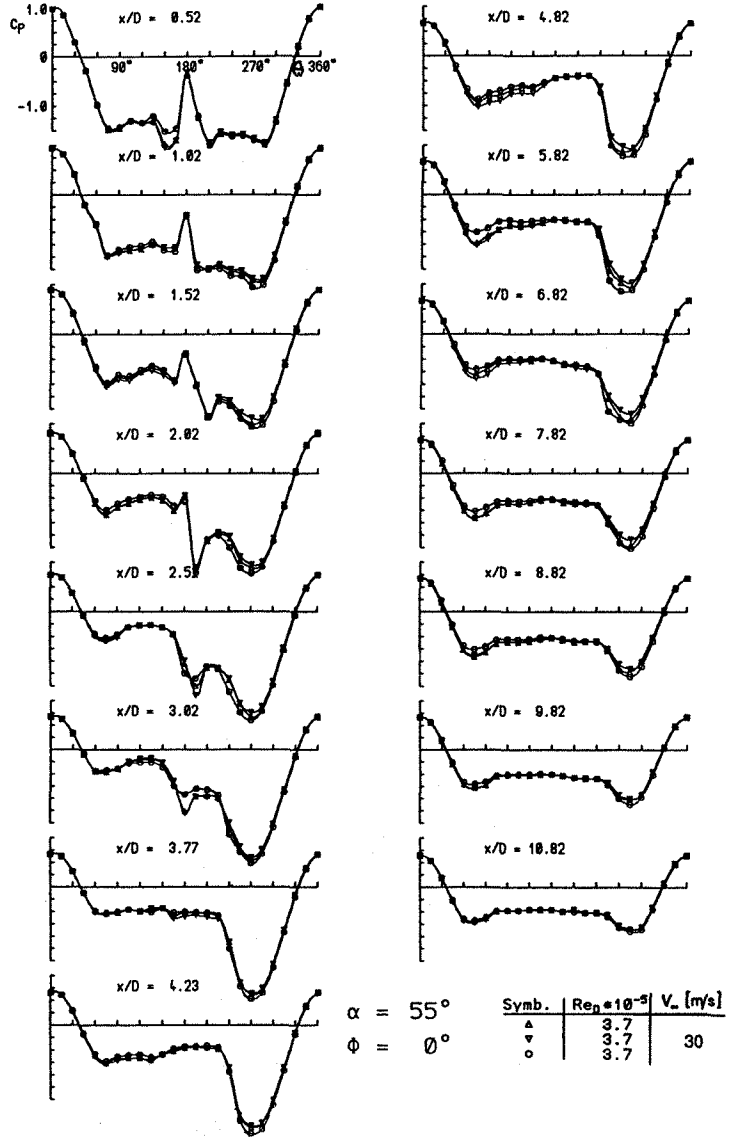

Fig. 11: Surface pressure distributions in 15 cross sections along the model. Results from the low speed wind tunnel NWB at Braunschweig

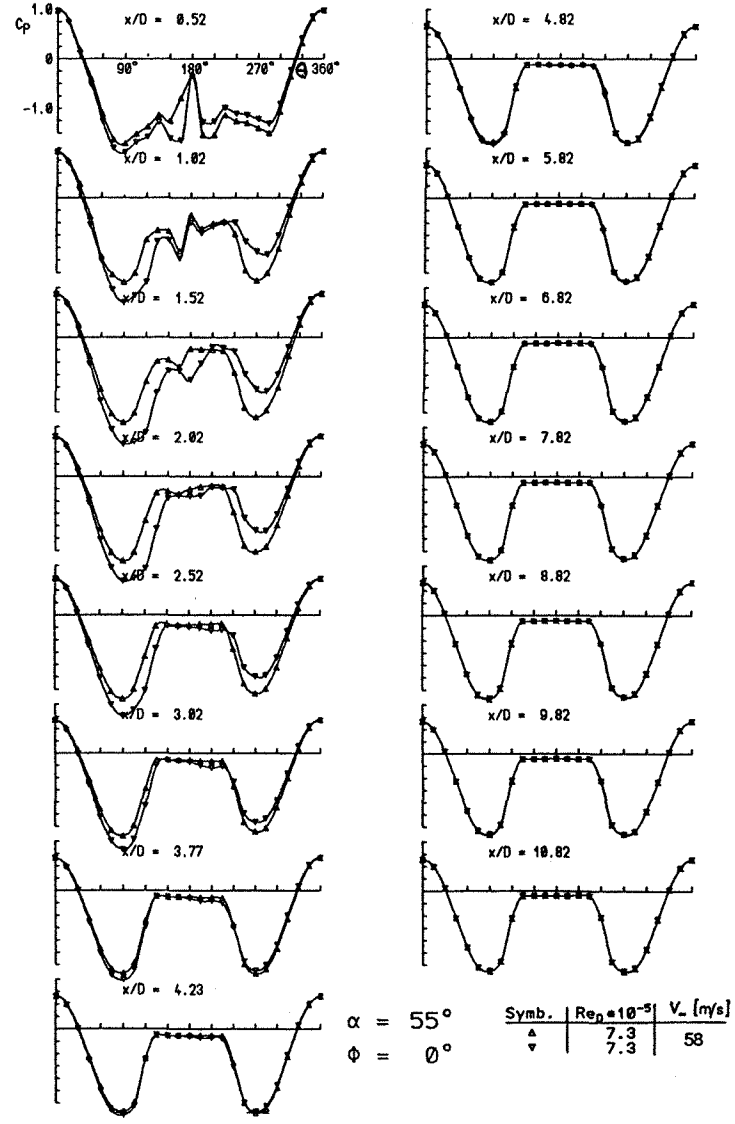

Fig. 12: Surface pressure distributions in 15 cross sections along the model. Results from the low speed wind tunnel NWB at Braunschweig

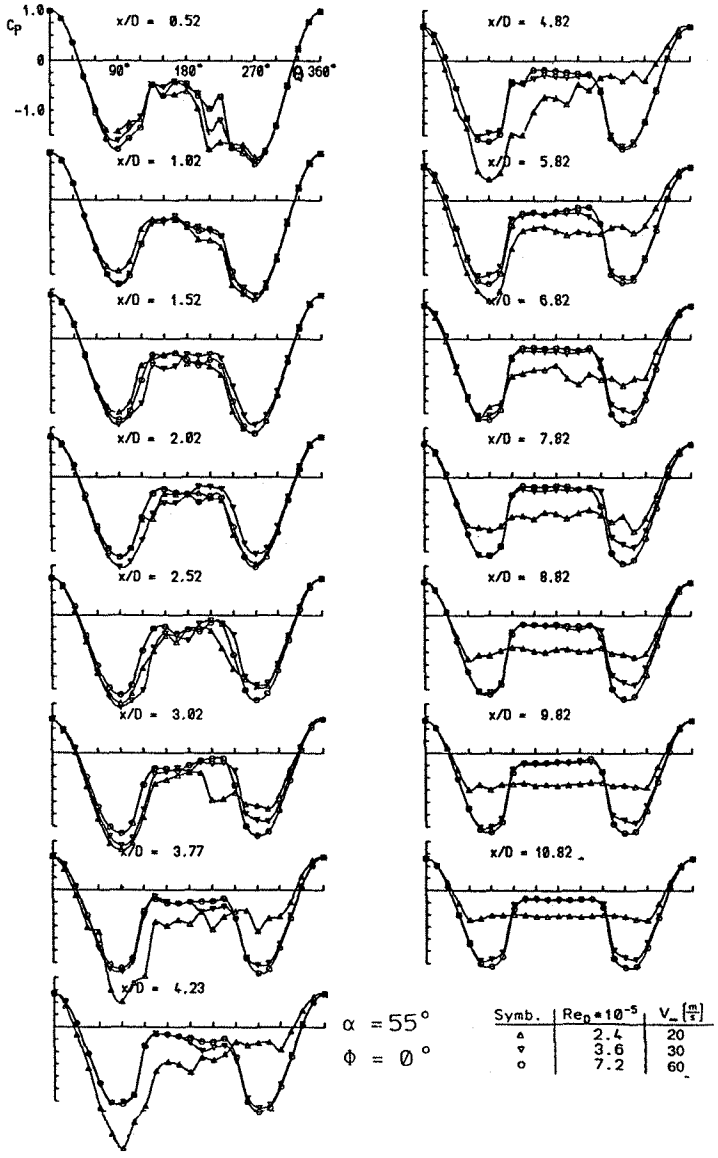

Fig. 13: Surface pressure distributions in 15 cross sections along the model. Results from the low speed wind tunnel NWG at Göttingen

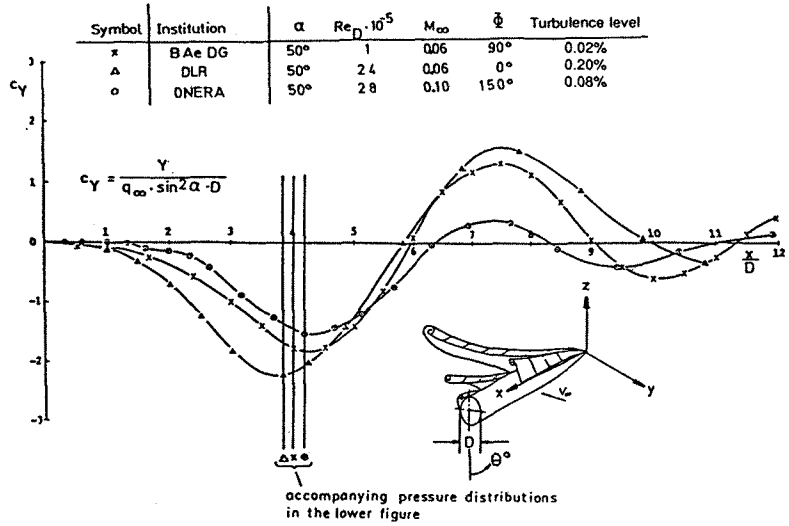

Fig. 14: Comparison of local side force distributions from BAe, DLR and ONERA. Figure prepared by J.R. Deane, BAe, U.K.

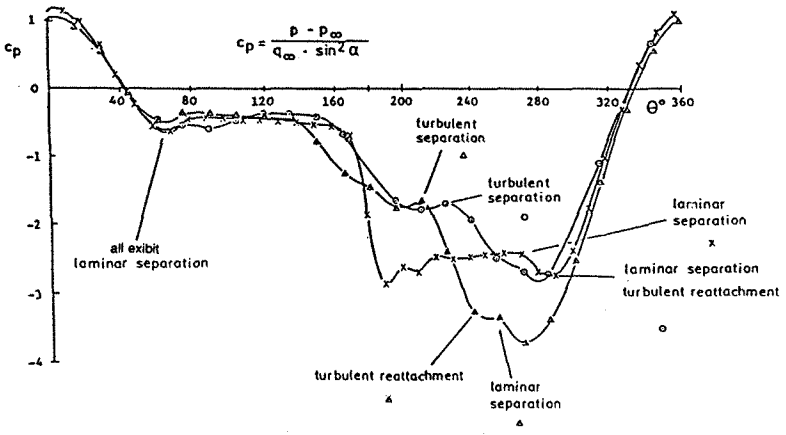

Fig. 15: Pressure coefficient distributions and important features. See indication in Fig. 14 Figure prepated by J.R. Deane, BAe, U.K.

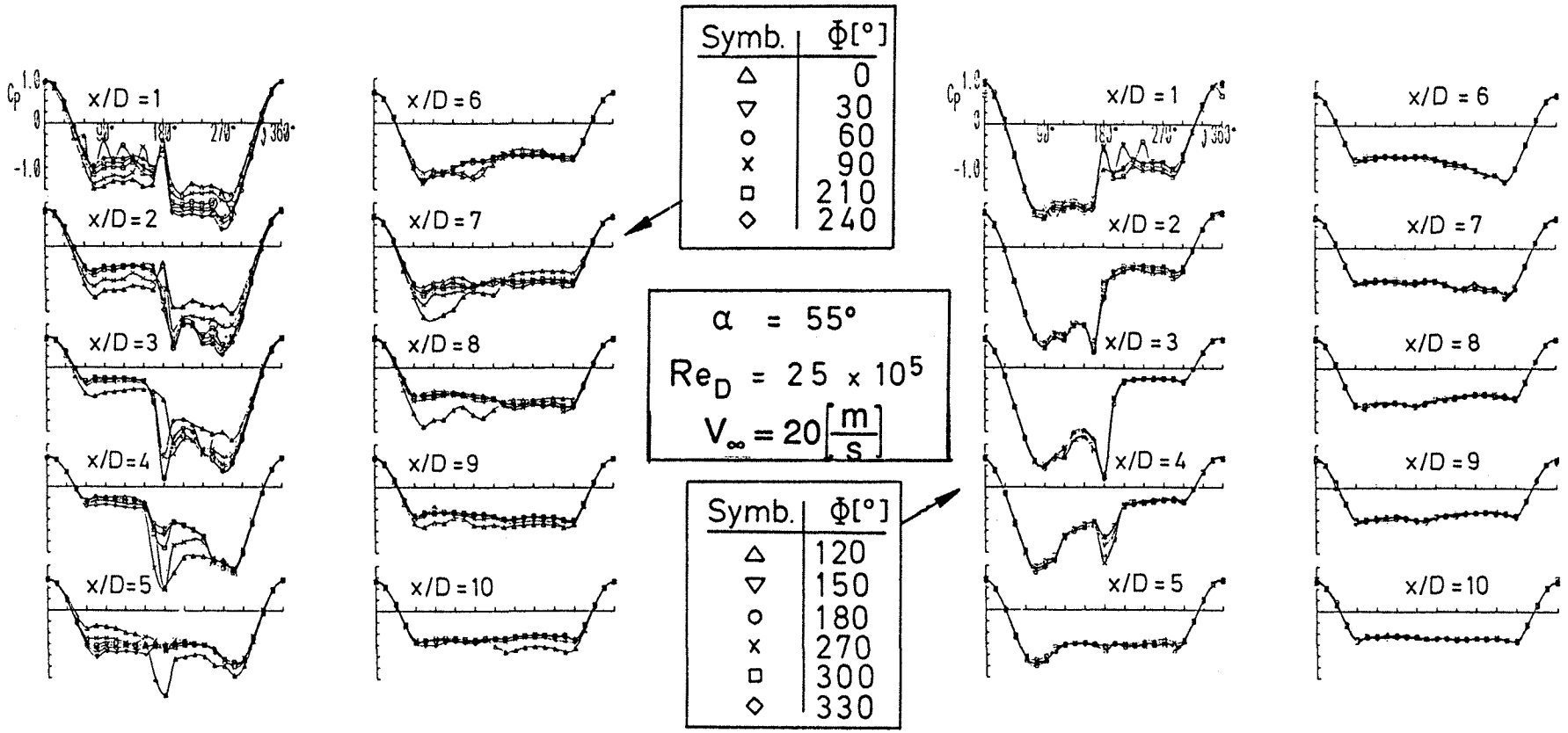

Fig. 16: Groups of pressure distributions of equal asymmetry

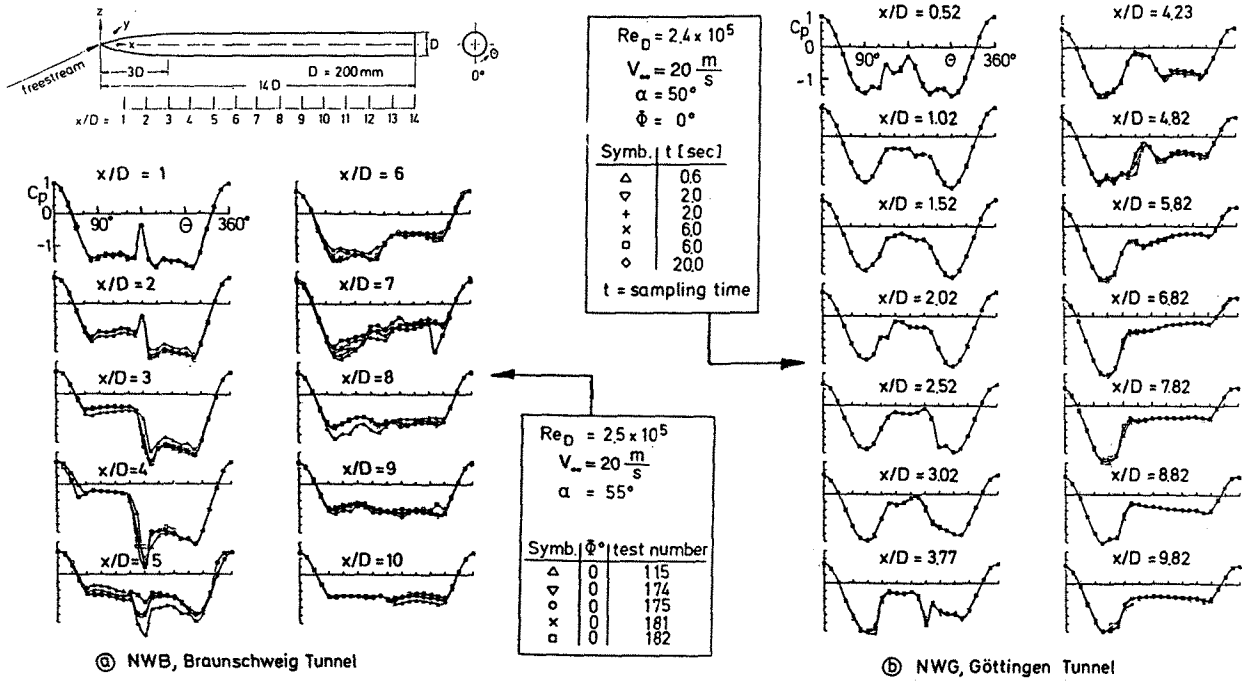

Fig. 17: Demonstration of the repeatability of the static surface pressure measurements

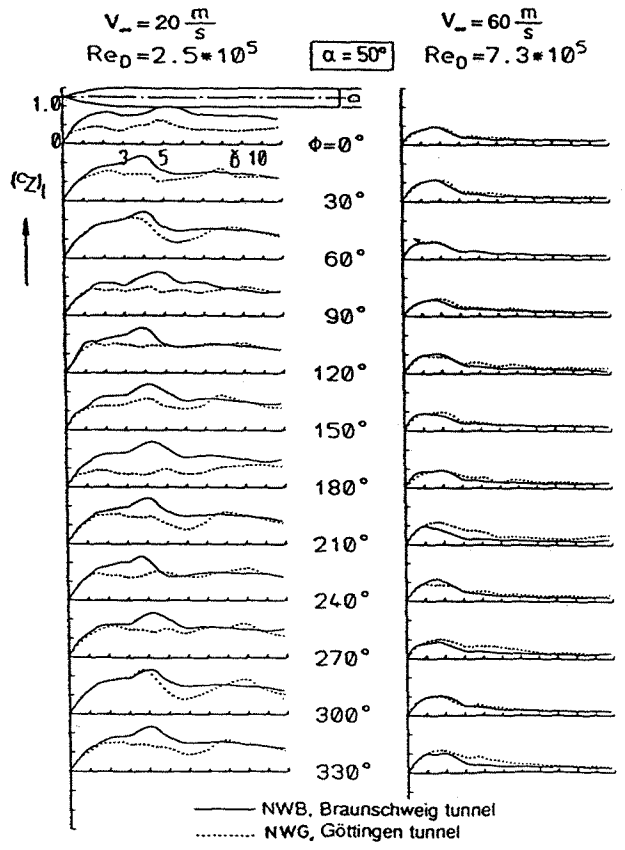

Fig. 18: Comparison of local normal force distributions derived from pressure data for different roll positions Φ at α = 55° and two Reynolds numbers in the wind tunnels at Göttingen and Braunschweig

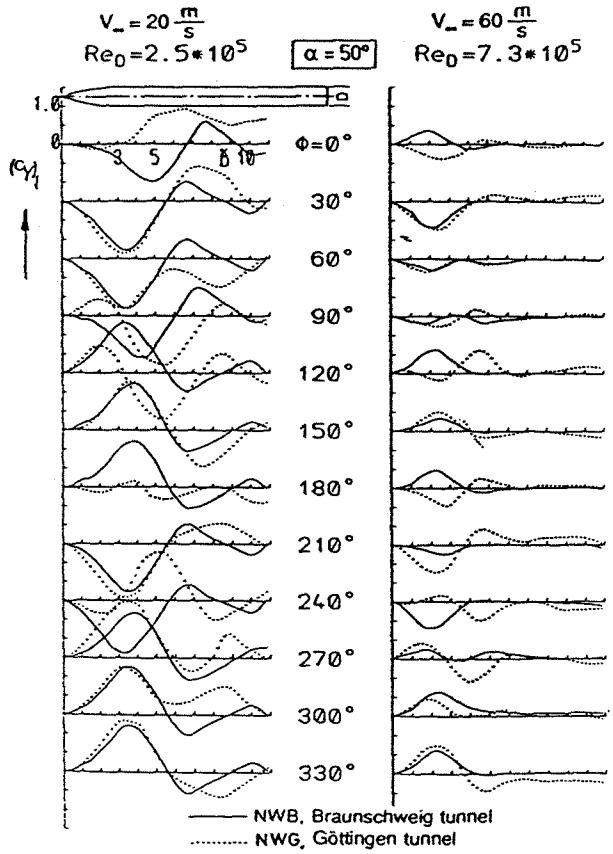

Fig. 19: Comparison of local side force distributions derived from pressure data for different roll positions Φ at α = 55° and two Reynolds numbers in the wind tunnels at Göttingen and Braunschweig

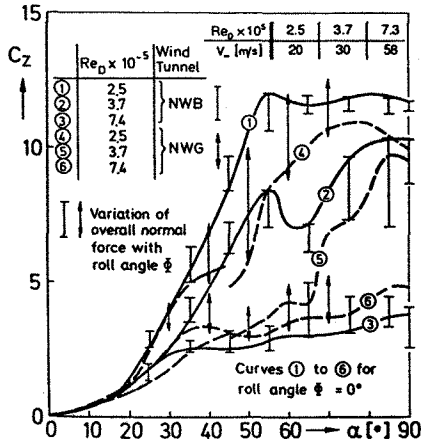

Fig. 20: Total normal force coefficients derived from pressure measurements

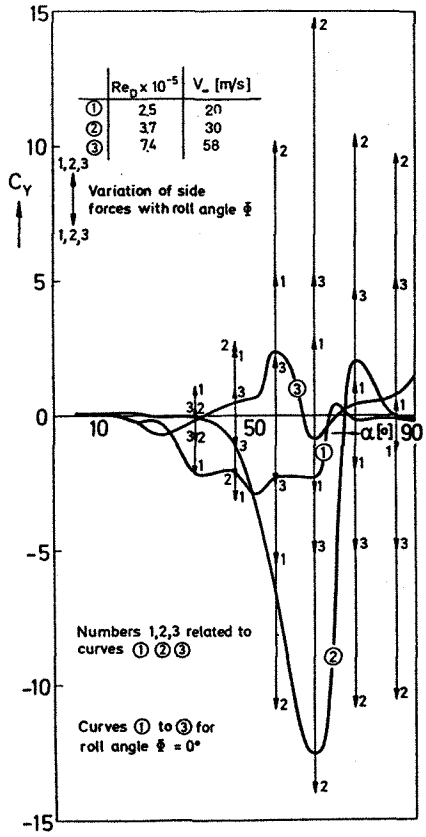

Fig. 21: Total side force coefficients derived from pressure measurements. Results from the Braunschweig tunnel, NWB

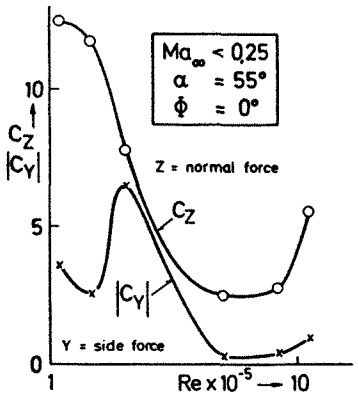

Fig. 23: Variation of total force coefficients with the Reynolds number

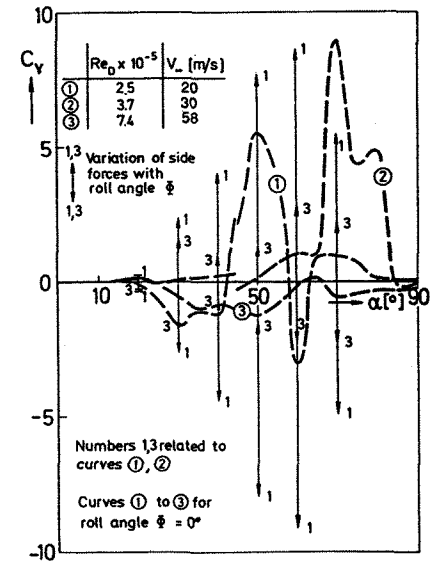

Fig. 22: Total side force coefficients derived from pressure measurements. Results from the Göttingen tunnel, NWG

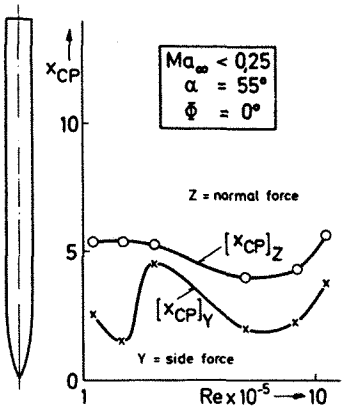

Fig. 24: Variation of centers of pressure with the Reynolds number

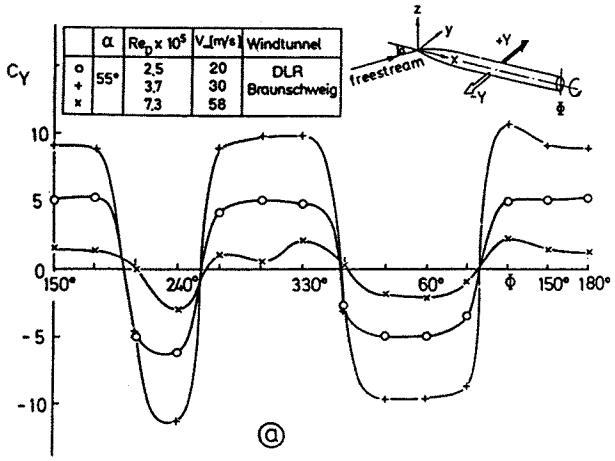

Fig. 25: Roll angle dependence of the total side force coefficients. Results from the Braunschweig tunnel

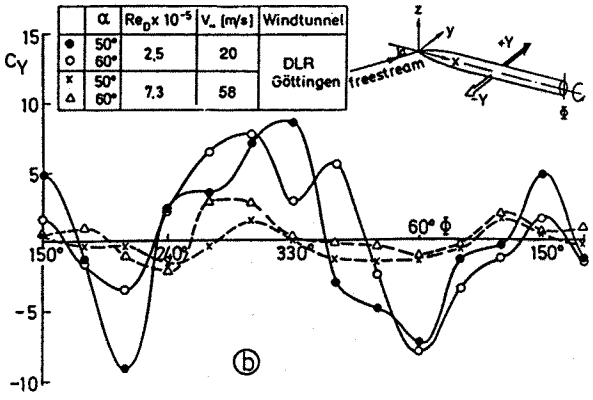

Fig. 26: Roll angle dependence of the total side force coefficients. Results from the Göttingen tunnel

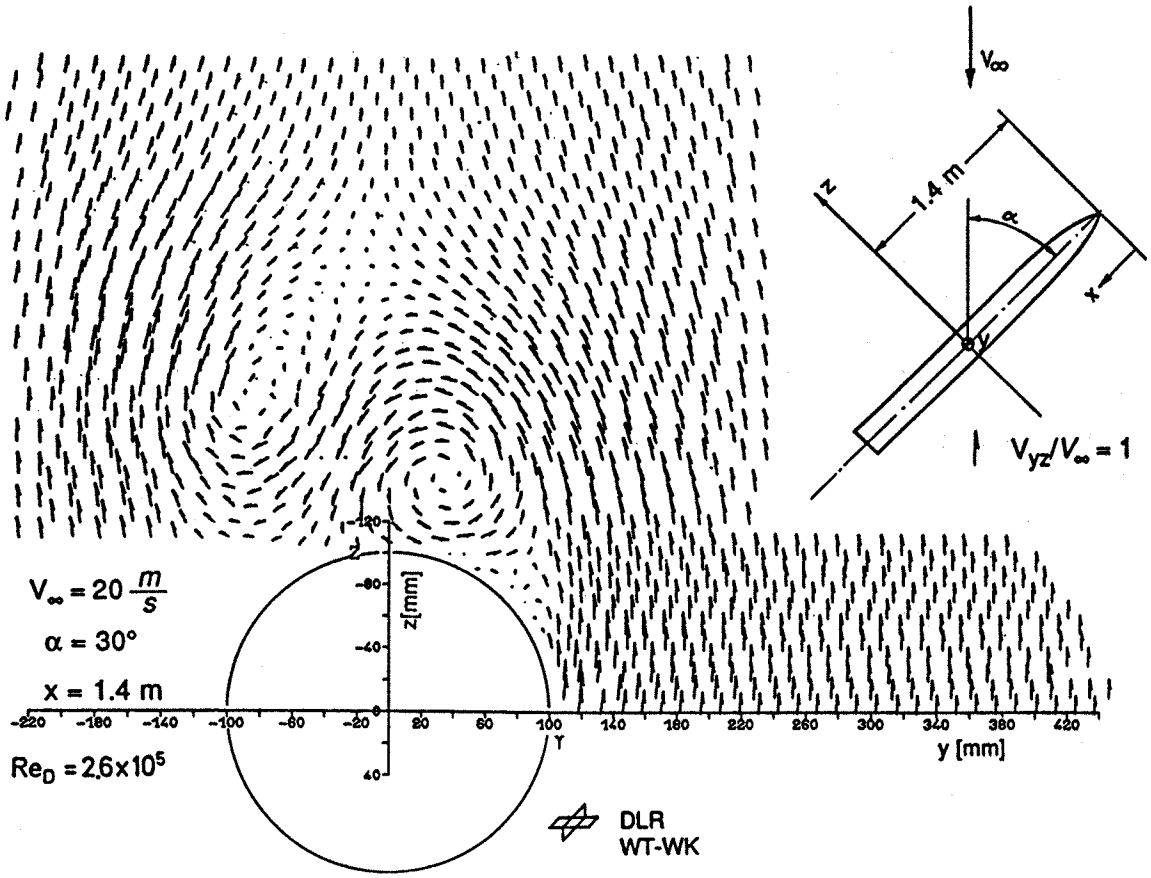

Fig. 27: Velocity vectors of the crossflow in the yz-plane at x/D = 7

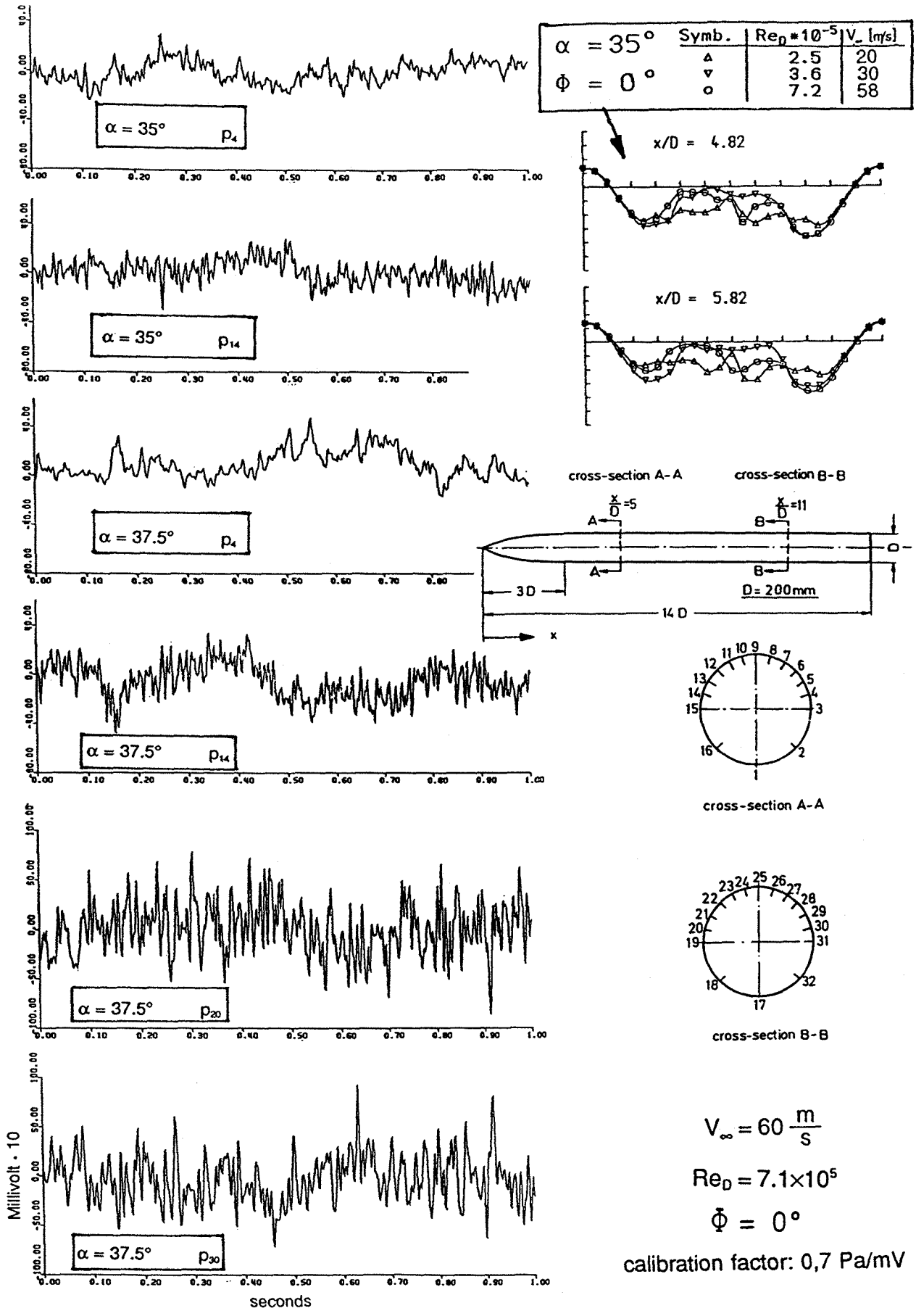

Fig. 28: Records of the dynamic part of the surface pressure at several pressure taps

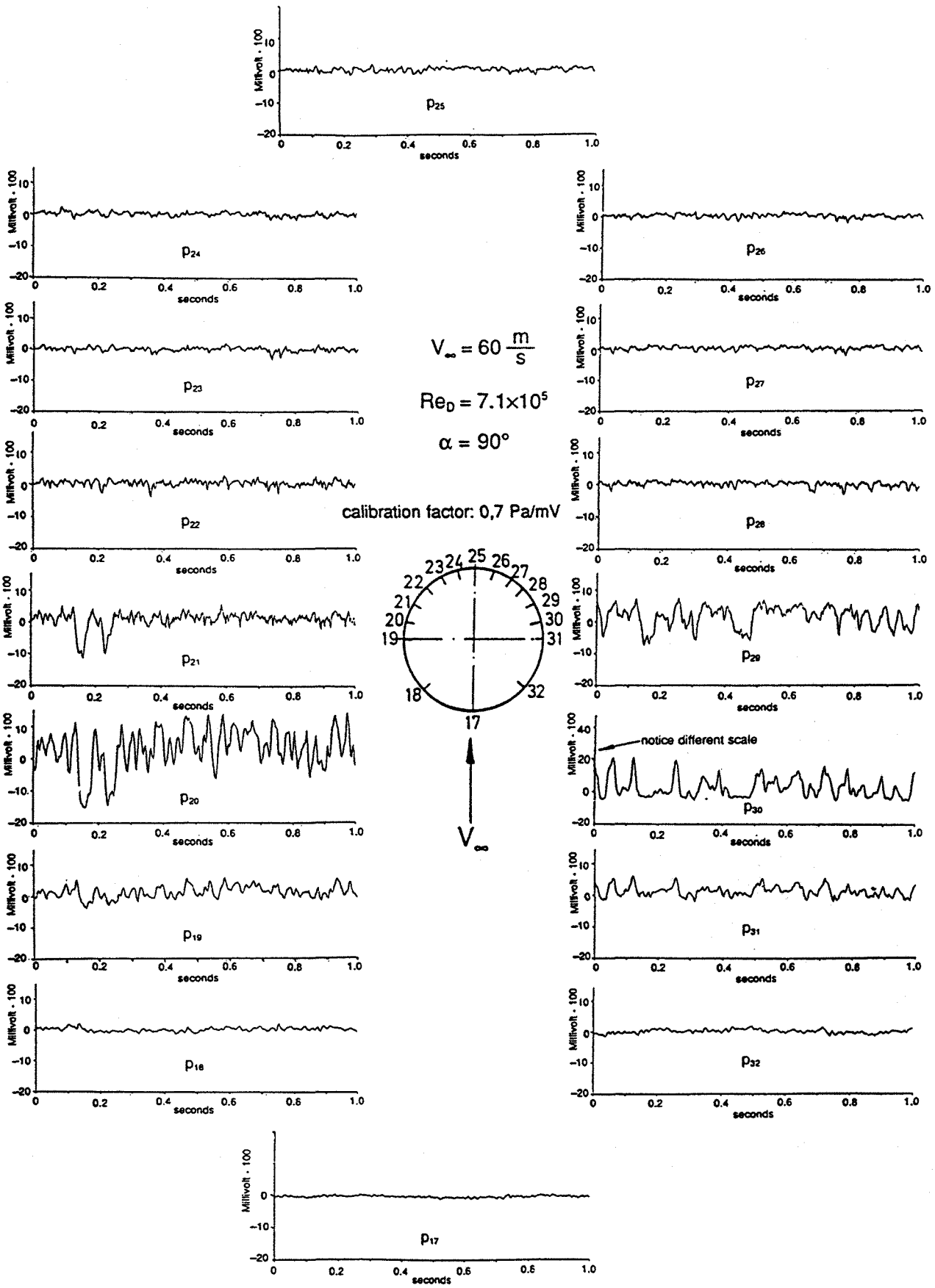

Fig. 29: Records of the dynamic part of the surface pressure at cross section x/D = 11 for 16 pressure taps around the body circumference

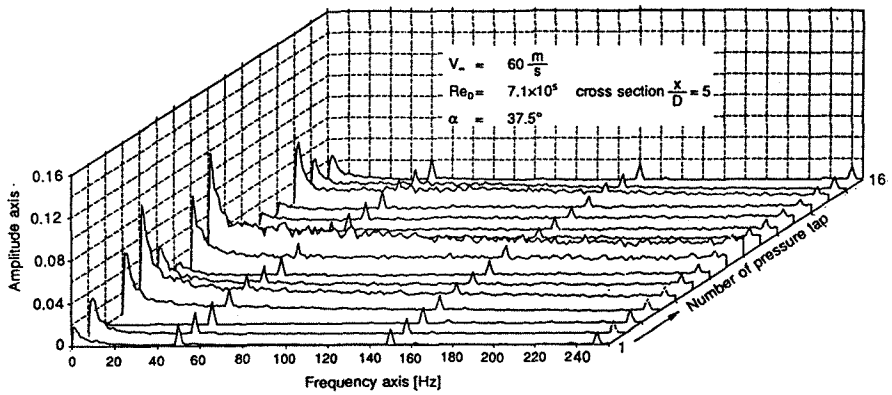

Fig. 30: Power spectra of the dynamic part of the surface pressure of the pressure taps 1 to 16 at body cross section x/D = 5, belonging to Fig. 26

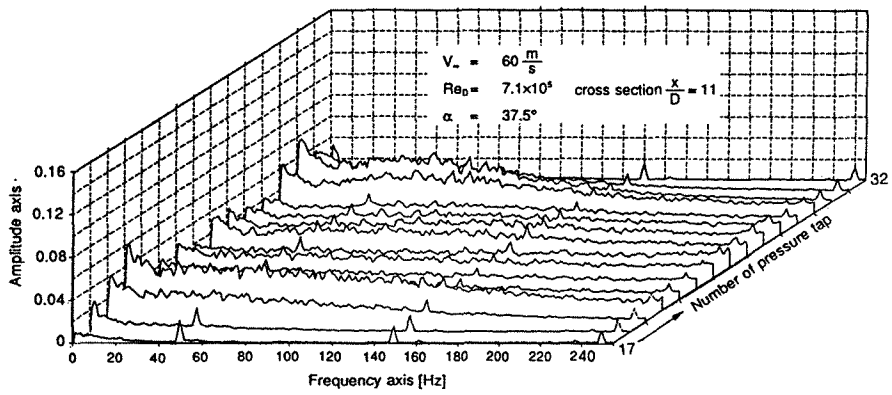

Fig. 31: Power spectra of the dynamic part of the surface pressure of the pressure taps 17 to 32 at body cross section x/D = 11, belonging to Fig. 26

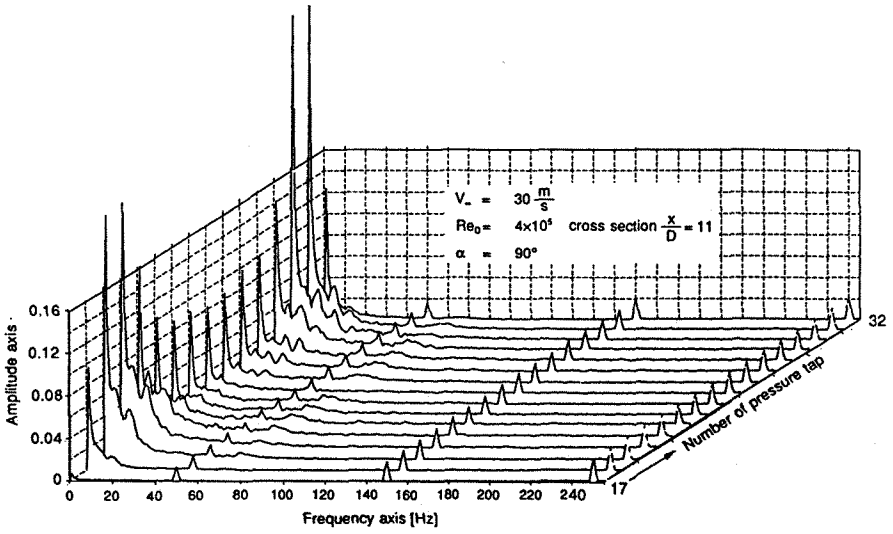

Fig. 32: Power spectra of the dynamic part of the surface pressure of the pressure taps 17 to 32 at body cross section x/D = 11, belonging to Fig. 27

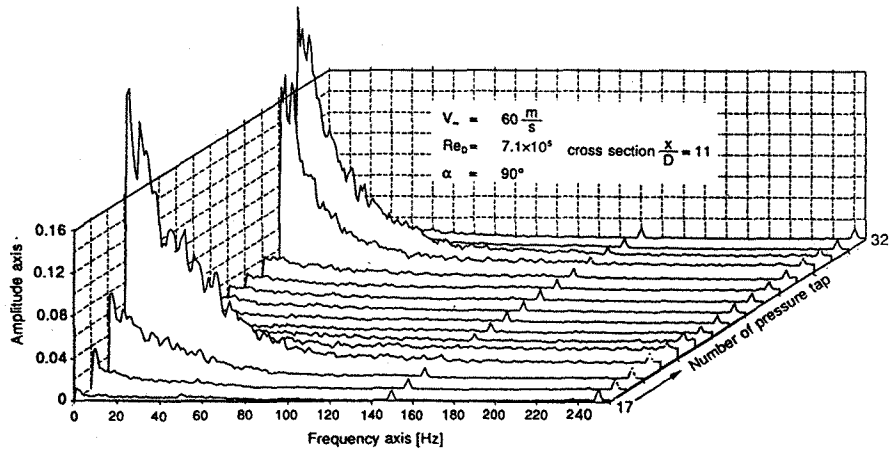

Fig. 33: Power spectra of the dynamic part of the surface pressure of the pressure taps 17 to 32 at body cross section x/D = 11, belonging to Fig. 27